

# PROCEEDINGS OF SPIE

[SPIDigitalLibrary.org/conference-proceedings-of-spie](https://SPIDigitalLibrary.org/conference-proceedings-of-spie)

## EUV flare and proximity modeling and model-based correction

Zuniga, Christian, Habib, Mohamed, Word, James, Lorusso, Gian, Hendrickx, Eric, et al.

Christian Zuniga, Mohamed Habib, James Word, Gian F. Lorusso, Eric Hendrickx, Burak Baylav, Raghu Chalasani, Michael Lam, "EUV flare and proximity modeling and model-based correction," Proc. SPIE 7969, Extreme Ultraviolet (EUV) Lithography II, 79690T (5 April 2011); doi: 10.1117/12.879488

**SPIE.**

Event: SPIE Advanced Lithography, 2011, San Jose, California, United States

# EUV Flare and Proximity Modeling and Model-based Correction

Christian Zuniga<sup>1</sup>, Mohamed Habib<sup>2</sup>, James Word<sup>3</sup>, Gian F. Lorusso<sup>4</sup>, Eric Hendrickx<sup>4</sup>,  
Burak Baylav<sup>4</sup>, Raghu Chalasani<sup>1</sup>, Michael Lam<sup>1</sup>

<sup>1</sup>Mentor Graphics Corp. 46871 Bayside Parkway Fremont, CA 94538

<sup>2</sup>Mentor Graphics Corp, 78 El Nozha St, Sbaa Emarat, Helipolis, Cairo, 11361, Egypt

<sup>3</sup>Mentor Graphics Corp. 8005 S.W. Boeckman Rd, Wilsonville, OR 97070

<sup>4</sup>IMEC, Kapeldreef 75, 3001 Leuven, Belgium

## ABSTRACT

The introduction of EUV lithography into the semiconductor fabrication process will enable a continuation of Moore's law below the 22 nm technology node. EUV lithography will, however, introduce new and unwanted sources of patterning distortions which must be accurately modeled and corrected on the reticle. Flare caused by scattered light in the projection optics is expected to result in several nanometers of on-wafer dimensional variation, if left uncorrected. Previous work by the authors has focused on combinations of model-based and rules-based approaches to modeling and correction of flare in EUV lithography. Current work to be presented here focuses on the development of an all model-based approach to compensation of both flare and proximity effects in EUV lithography. The advantages of such an approach in terms of both model and OPC accuracy will be discussed. In addition, the authors will discuss the benefits and tradeoffs associated with hybrid OPC approaches which mix both rules-based and model-based OPC. The tradeoffs to be explored include correction time, accuracy, and data volume.

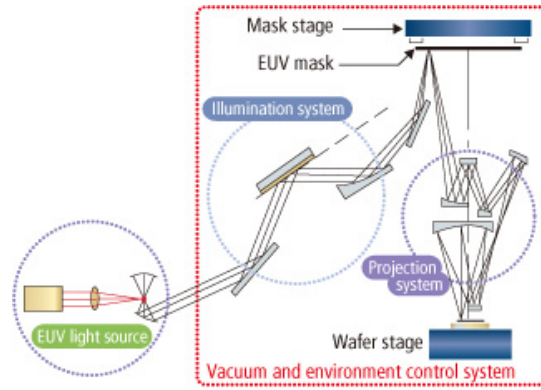
**Keywords:** EUV, model, flare, shadowing, OPC

## 1. Introduction

Extreme Ultraviolet Technology offers the capability of extending Moore's law beyond the 22 nm node<sup>1, 2</sup>. The ten times reduction in wavelength in EUV can bring  $k_1$  back up to 0.5 or above. This technology still faces many challenges however, primarily in the needed source power, resist characteristics, and availability of defect free masks<sup>3</sup>.

Although the imaging becomes easier with EUV, there is a need to correct for flare and shadowing<sup>4</sup>. Flare increases rapidly with decreasing wavelength; thus it is more prominent for EUV than in DUV systems. Shadowing arises from the off-axis illumination of the mask as shown in Figure 1. Left uncorrected, both flare and shadowing worsen the CD uniformity.

In this paper, we show how flare and shadowing are modeled and corrected in Mentor Graphics' Calibre software. Sections 2.1 and 2.2 explain how the flare and shadowing effects are modeled by Calibre, respectively. In Section 3 we show an example of using the flare model. Finally, Section 4 shows how the correction is done using the model.



Source: EUVA website (<http://www.euva.or.jp/>)

**Figure 1 Schematic of an EUV System**

## 2.1 Modeling for EUV Flare

Flare in EUV systems is caused by surface roughness in the mirrors<sup>5,6</sup>. Incident light is scattered in multiple directions in addition to the specular direction as shown in Figure 2. Flare is more prominent in EUV systems because of two main reasons. First, the amount of scattering is inversely proportional to the wavelength squared. Second, for reflections, the light must travel twice across the interface.

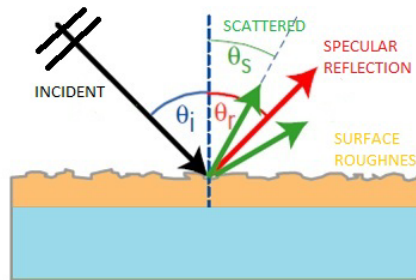


**Figure 2 EUV light scattering from surface roughness**

The scattering is captured by the power spectral density (PSD). The final effect on the aerial image is modeled by the pedestal model shown in Equation 1.

$$I_F = (1 - TIS)I_0 + I_0 \otimes FPSF \quad (1)$$

The factor  $I_0$  accounts for the effects of the partial coherence. TIS is the total integrated scatter or the overall flare. The overall energy available for coherent image formation is decreased to the amount  $1 - TIS$ . The local flare is obtained by convolving the flare PSF (FPSF) with the intensity  $I_0$ .

The flare PSF is the flare response of a point source. It can be obtained by Kirk test patterns or from the PSD in the optics. The scattering into the mid-spatial frequency makes it a very long range function ranging from a few hundred nanometers to several millimeters. It can be approximated by a fractal form as shown

in Figure 3. Several fractals will most likely be required to approximate it well, however. The TIS can be found by integrating the PSF over the brightfield area.

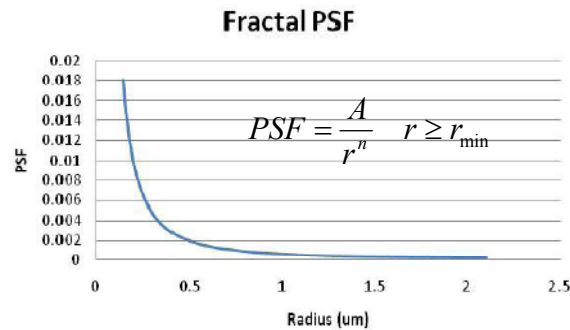


**Figure 3 Single fractal kernel**

The long range of the flare PSF makes it impractical to compute the flare for OPC with a direct convolution of the aerial image with the PSF. However, it has been found that convolving the PSF with an average mask density grid can give enough accuracy<sup>7,8</sup>. Variable size grids are also needed to speed up computation. Figure 4 describes this flow in calculating the flare. The original layout is first divided into a coarse, 1  $\mu\text{m}$  grid layout and the layout density is calculated. The grid is then convolved with either the flare PSF or the measured PSF values to produce a flare map. The flare map stores the flare as a function of position, assigning a flare value to a non-overlapping region. This flare value is used to modulate the intensity according to Equation 2.

$$I_F = (1 - TIS)I_0 + F(x, y) \quad (2)$$

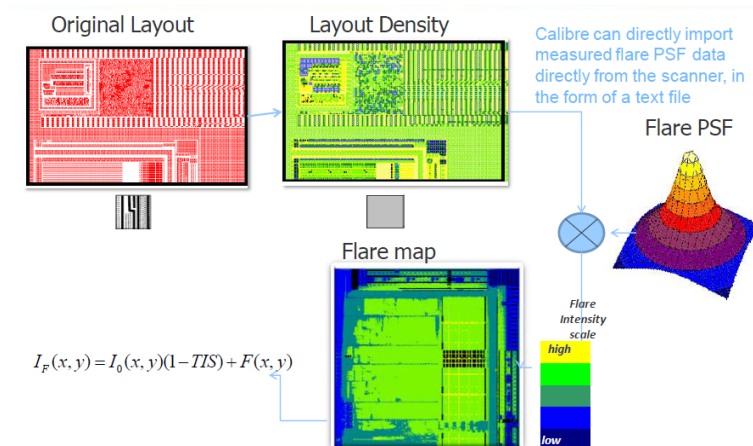


**Figure 4 Calculation of flare map**

## 2.2 Shadowing Model

An EUV system is non-telecentric on the mask side<sup>10</sup>. The mask is illuminated by the light at an inclination angle of  $6^\circ$  and varying azimuthal angles ranging from  $0$  to  $\pm 22^\circ$  as shown in Figure 5. This causes a feature to print differently depending on its orientation and angle of incidence. Figure 6 for example shows that horizontal lines print larger than  $42\text{ nm}$  vertical lines. For larger features and pitches, a simple global bias on horizontal edges can simulate the shadowing effect. This was the approach taken for the modeling

example in the next section giving reasonable accuracy. For tighter nodes, a model-based shadowing will be needed<sup>9</sup>.

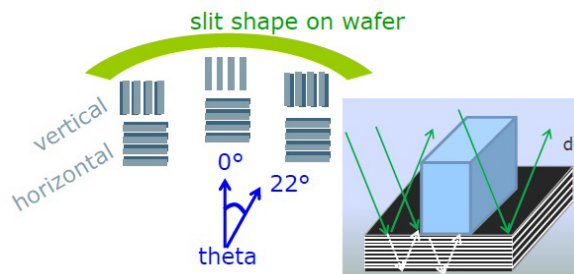


**Figure 5 Mask is illuminated from an off-axis source**

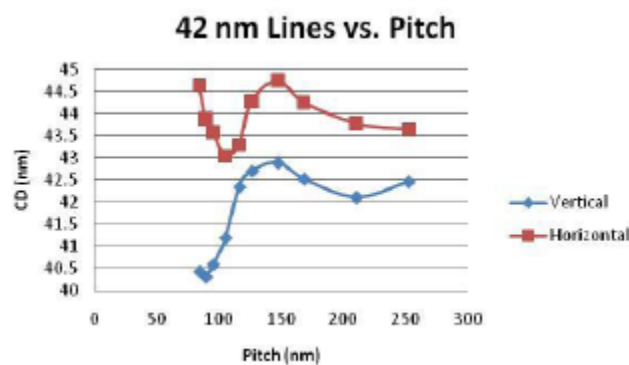


**Figure 6 Measured vertical and horizontal 42 nm lines vs. pitch**

Shadowing is modeled more accurately by extending edge DDM methods to handle reflective multilayer EUV masks. DDM was introduced to quickly handle 3D masks effects<sup>11</sup>. Figure 7 shows the concepts behind DDM. The field transmitted by a mask opening can be decomposed into the sum of the responses of the edges. The actual intensity in the image plane can then be well approximated by adding perturbation signals to a Kirchhoff mask. The perturbation signals are the edge responses to different field polarizations calculated from a rigorous Maxwell solver. In the EUV case, the mask is reflective instead of transmitting. Finally, the off-axis illumination is modeled by a hybrid Hopkins-Abbe model similar to the one described in Reference 12.

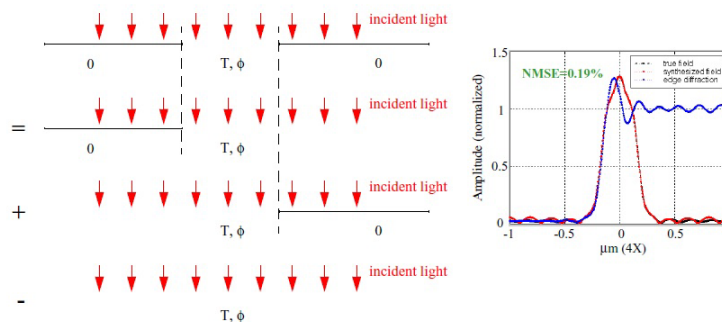


**Figure 7 Principle of DDM for modeling 3D mask effects.**

### 3. Model Calibration with Flare and Shadowing

Calibrating a model with flare and shadowing is not very different from traditional OPC calibration. Figure 8 shows the steps involved. First the flare map is calculated using either a measured PSF file or fractal kernels. Then a global bias is applied to account for shadowing. An initial estimate of this bias can be obtained from the measured printed difference between vertical and horizontal orientations of identical features. The intensity accounting for the partial coherence is calculated with the regular OPC engine and modulated by the flare model. The intensity with flare is then used as an input to the resist model that outputs the simulated CD. Standard CM1 models can be used for the resist model. The model and bias giving the lowest error is then selected.

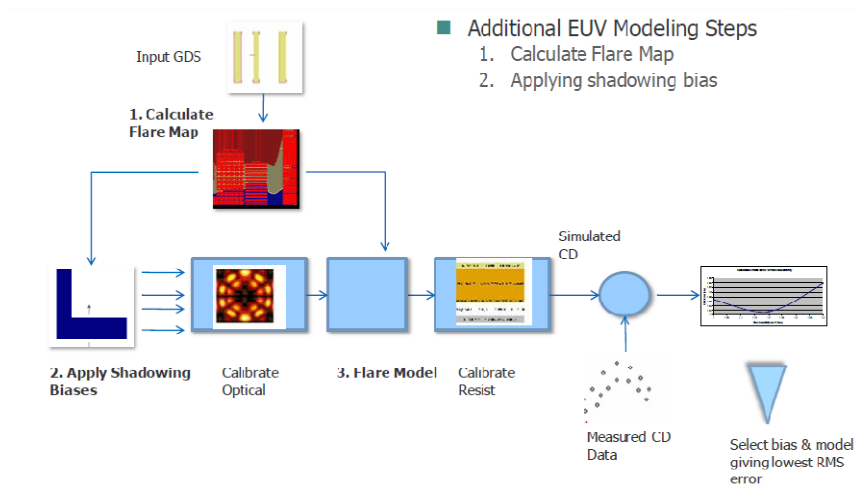


**Figure 8 Model calibration flow with flare and shadowing**

We tested the flare model using a data set provided by IMEC and taken from the alpha-demo tool. The set consists of the features listed in Figure 9 and includes lines through pitch, MEEF, and line ends. Most of these features were exposed at different flare levels and using both vertical and horizontal orientations. Figure 10 shows there are three general flare levels with 2% flare in the middle, 4% in the top, and 6% in the bottom. The data clearly shows the effects of flare and shadowing. Figure 11 shows a sample set of 36 nm lines with increasing pitch. As expected as the flare increases, the line width decreases. Overall lines change by about 1nm per percentage increase in flare. Figure 12 shows the horizontal lines print larger than the vertical lines by about 2 nm.

Feature type	CD range (nm)	Pitch range (nm)	Module	Count
H/V lines-proximity	36-46	72-276	Top	120
H/V lines-MEEF	32-50	70-270	Top	116
H/V iso spaces	32-45	245-280	Top	36
H/V EOL	40-100 gap CD	80-320	Top	32
H/V lines-proximity	36-46	72-276	Mid	120
H/V iso spaces	32-45	245-280	Mid	36
H/V lines-proximity	36-46	72-276	Bottom	120
H/V iso spaces	32-45	245-280	Bottom	36

**Figure 9 Feature types available in IMEC data set**

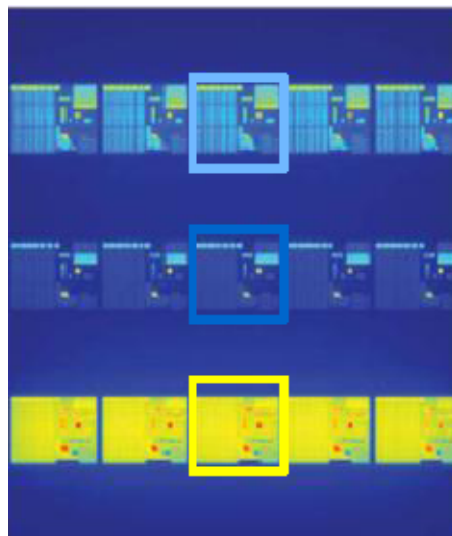


**Figure 10 Flare map of IMEC example showing 3 general flare levels.**

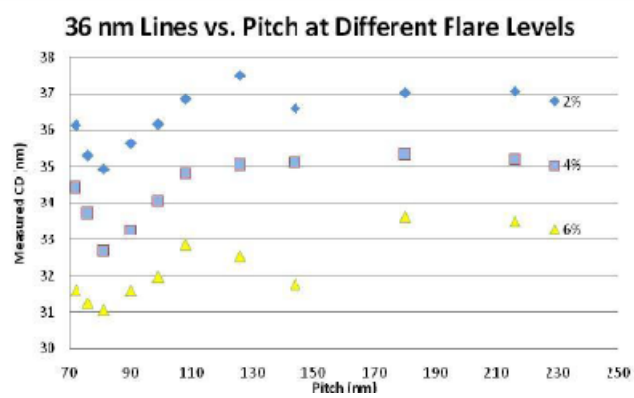


**Figure 11 Sample 36 nm lines at the 3 flare levels.**

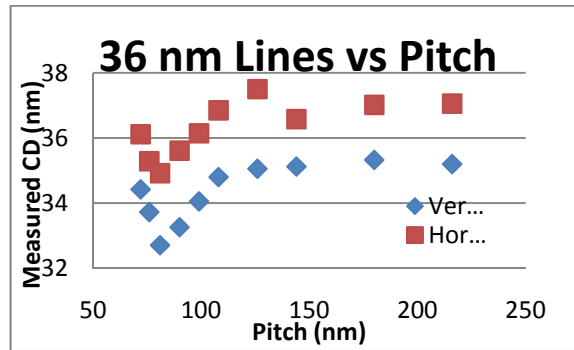


Figure 12 Sample 36 nm lines in vertical and horizontal orientations

Initially, we calibrated the models to all the data at once, including data at all three flare levels and in both orientations. We compared two flare models. One used a single fractal that was calibrated to the measured flare values<sup>13</sup>. The other one used a double fractal obtained from the optics. Table 1 summarizes the modeling errors with and without the flare model. The model with no flare has an RMS error about 1nm higher than the models with flare. Without flare information, the model is unable to track the change in CD seen in Figure 11. The best the model can do is to try to fit the data at the middle flare level and the model error agrees well with the deviation of the two other levels from the middle flare level. The two flare models show almost no difference in the RMS error and have comparable values to the errors reported previously for this case<sup>14, 15</sup>.

Table 1 Calibration results with all the data

RMS Errors (nm)	No Flare	Single Fractal*	Double Fractal**
ALL DATA	2.24	1.12	1.13

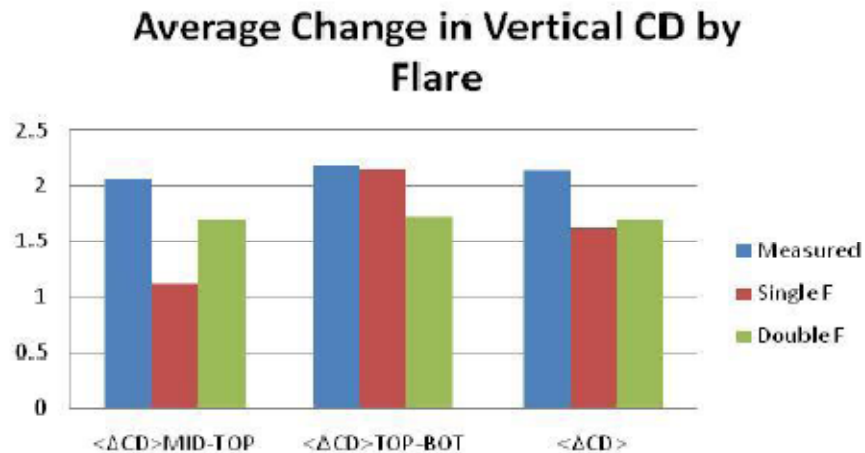
To test the models' predictive ability, we used the data from the top and bottom for calibration and verified the resulting models on the data from the middle region. Table 2 summarizes the model errors. The model with no flare loses accuracy when applied to the verification set. The models with flare are able to maintain approximately the same RMS error. In this test, the double fractal flare model showed slightly better predictive ability.



**Table 2 Calibration and verification results with and without the flare models**

RMS Errors (nm)	No flare model	Single Fractal	Double Fractal
Calibration on TOP and BOT	1.68	1.05	1.15
Verification on MID	3.32	1.28	1.16

Although the models with flare can give a lower error than without flare, it is also important to determine how accurate the flare model is. A simple way of doing this is by comparing the predicted change in CD from the models with the measured change in CD. Figures 13 and 14 show the average change in CD for vertical and horizontal lines in going from the middle to the top region and from the top to the bottom region. Although there are some differences in the predicted change from one region to the other, overall the models give a change in CD within 0.5 nm of the average measured change. Both the single and the double fractal model give comparable values. These results indicate the flare is being modeled with reasonable accuracy. Even greater accuracy may be required for future nodes however.

**Figure 13 Summary of the average change in CD for vertical lines**

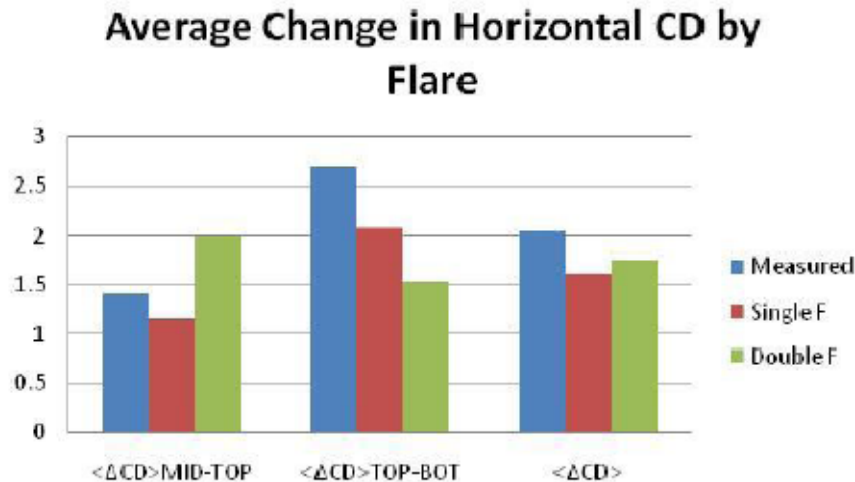


Figure 14 Summary of the average change in CD for horizontal lines

#### 4. Correction

The calibrated flare-aware resist model and shadowing-aware optical model were then used for development of an OPC flow within the Calibre OPC framework. The first step we took was to conduct some experiments to determine the best simulation engine in terms of run time. Two simulation engines are available, each uniquely suited to different tasks depending on factors such as layout density and illumination conditions.

Sparse simulation, where images are computed only where needed and in the spatial domain, was the most efficient method for computing images at the 65 nm node and above<sup>16</sup>. The simulation run time is highly sensitive to layout density, and relatively insensitive to illumination parameters NA,  $\sigma$ , and  $\lambda$ . Dense simulation, where images are computed everywhere across the chip in the frequency domain, has become the most efficient method at the 45 nm node and below<sup>17</sup>. In contrast to sparse, dense simulation is highly sensitive to NA,  $\sigma$ ,  $\lambda$ , and relatively insensitive to layout density.

In order to determine which is faster at the 22nm and 16nm nodes with EUV illumination conditions we conducted experiments based on shrinks of 32nm-node active, poly, contact, and metal logic design layouts. Illumination conditions were chosen based on currently available alpha demo tools (NA = 0.25,  $\sigma$  = 0.5) and possible future production tools (NA = 0.4,  $\sigma$  = 0.95). The results are plotted in Figures 15 and 16. The results clearly show the advantages of sparse simulation in nearly every case, except for NA = 0.25, 22nm Metal 1 where dense is slightly faster than sparse.

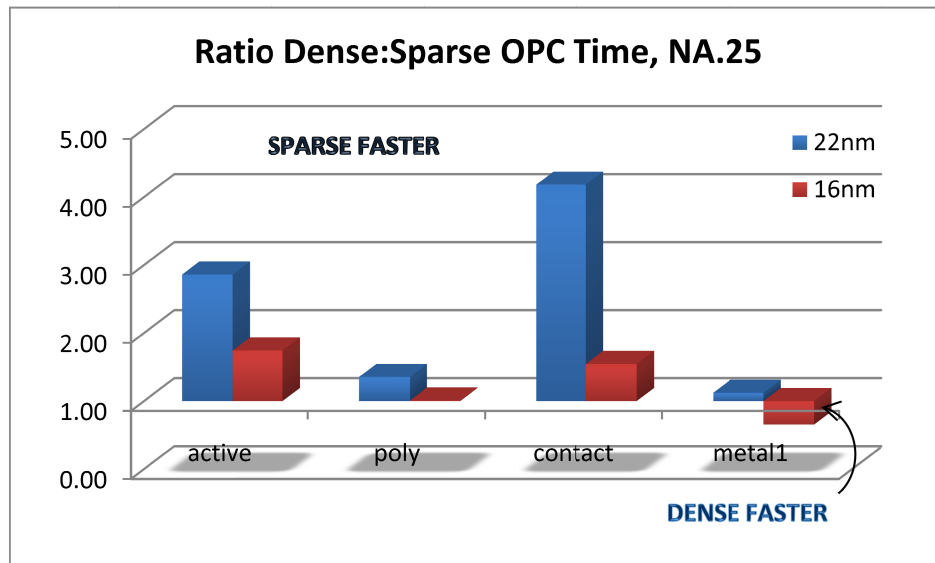


**Figure 15** Ratio of sparse: dense simulation time for 22nm and 16nm active, poly, contact, and metal layers with NA=0.25,  $\sigma = 0.5$

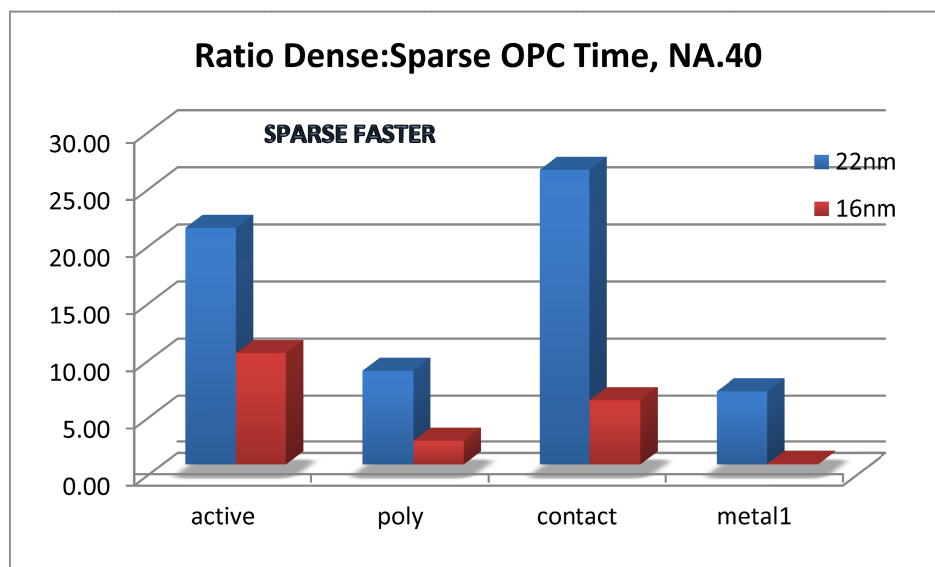


**Figure 16** Ratio of sparse: dense simulation time for 22nm and 16nm active, poly, contact, and metal layers with NA=0.4,  $\sigma= 0.95$

We next sought to determine the impact on design hierarchy after correction, of adding flare and mask shadow models to the OPC engine. Design hierarchy allows for tremendous compression of both layout file size and correction run time, especially for highly regular memory designs. For these experiments we chose a DRAM Poly layer. The plot in Figure 17 shows the impact of flare and mask shadow models on runtime, post-OPC hierarchical compression ratio, and post-OPC file size. Note that for runtime and file size we want smaller numbers, and for the flat: hierarchical compression ratio, bigger is better. The results show that the impact of the additional EUV models for flare and mask shadowing are driving an increase in both correction time and post-OPC file size of around 2X. Part of the correction time increase can be attributed to the extra simulation time for the flare and mask shadowing as well as loss of hierarchical

compression caused by the very long interaction range of the flare model. The increased file size can be attributed almost solely to the loss of hierarchy.

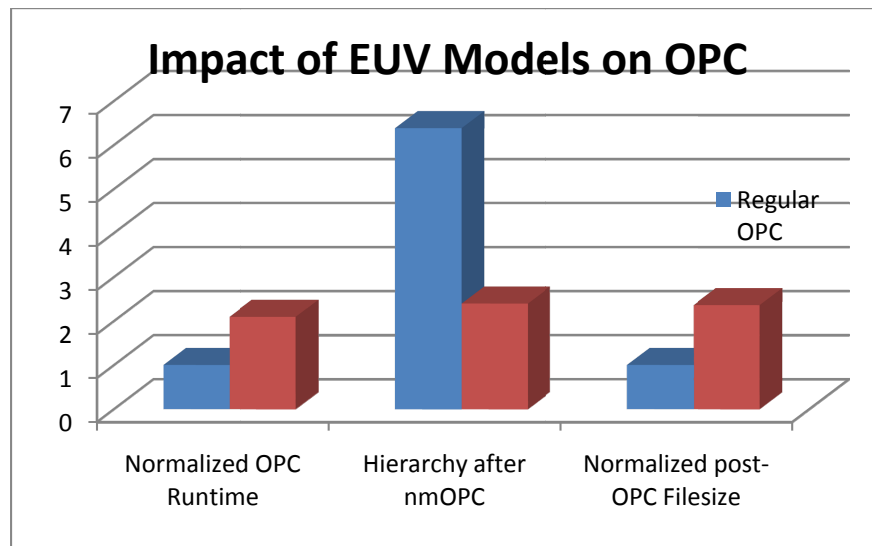


**Figure 17** The impact of adding flare and mask shadowing on EUV OPC (normalized) run time, hierarchical compression ratio, and (normalized) post-OPC file size

For the accuracy of the OPC correction algorithms for flare and shadowing, studies are still underway. It is clear from an examination of pre-OPC and post-OPC simulated contours and mask shapes that the results are qualitatively correct. To demonstrate this we show in Figure 18 the pre-OPC mask shapes (which are 25nm X 65nm isolated posts) and pre-OPC aerial images and resist contours. The images show the expected image shifting and biasing depending on orientation as well as location within the scanner field.

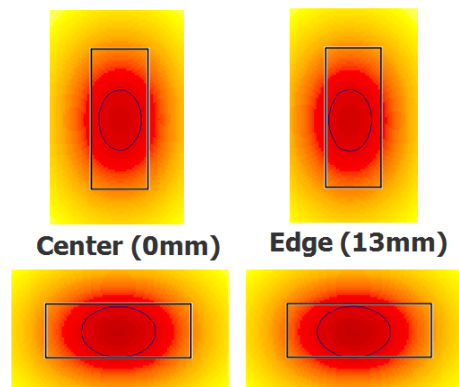


**Figure 18** Pre-OPC mask shapes, aerial images, and contours for a 25nm X 65nm isolated post, in both horizontal and vertical orientations, and at the center and extreme edge of the scanner field.

Finally in Figure 19 we show the resulting mask biases applied to the same shapes. The magnitude and direction of the bias make sense qualitatively given the nature of the mask shadowing effects. Quantitative confirmation of the accuracy of our mask shadowing model will occur pending available wafer data.

Post-OPC Mask Biases (nm)								
Scanner Slit Location (mm)	Horizontal				Vertical			
	bias1	bias2	bias3	bias4	bias1	bias2	bias3	bias4
13	2.7	1.8	14.8	15	3.1	3.5	14.2	13.3
0	2.7	1.8	15.1	14.9	3.7	3.4	14.2	13.3

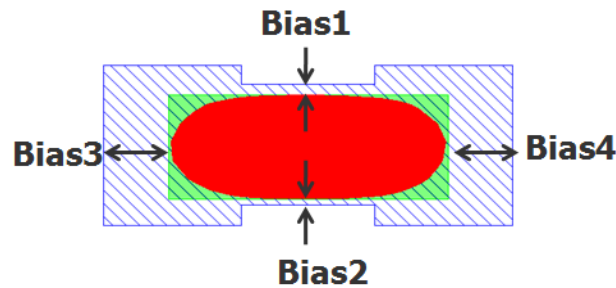


**Figure 19** Post OPC mask shapes for a 25nm X 65nm isolated post, in both horizontal and vertical orientations, and at the center and extreme edge of the scanner field.

## 5. Summary

In this paper, we have shown how flare and shadowing are modeled in Calibre's nmOPC software. Flare is modeled by a flare map, obtained from a convolution of the layout density with a flare PSF. The flare PSF can be either measured with Kirk-like test patterns or obtained from the optics. The flare is then used to directly modulate the intensity. The resist model is applied to this modulated intensity to obtain the CD. We tested the flare model on an existing data set from the alpha-demo tool and obtained good modeling errors. Future work will consist in more accurately modeling the flare PSF and shadowing.

On the correction side, we determined that using sparse simulation may actually be advantageous for the 22 and 16 nm nodes. For a typical DRAM layout, the additional EUV models for flare and mask shadowing increased both correction time and post-OPC file size by approximately 2X. The long interaction range of the flare model causes a loss in the hierarchical compression. Quantitative analysis of accuracy of the OPC correction algorithms for flare and shadowing effects are still underway, but qualitative results look very promising.

## REFERENCES

- [1] Wood, Koay, et. al "Integration of EUV Lithography in the fabrication of 22 nm node devices" Proc. of SPIE Vol. 7271 727104 2009
- [2] H. Aoyama, Y Tanaka, et. al. "Applicability of extreme ultraviolet lithography to fabrication of hp-35nm interconnects", Proc. of SPIE Vol. 7636, 2010.
- [3] Lin "Sober view on extreme ultraviolet lithography" J. Microlithography, Microfabrication, and Microsystems Vol. 5(3) July-Sep 2006
- [4] G. Lorusso, E. Hendrickx et. al., "Full Chip Correction of EUV Design", Proc. of SPIE Vol. 7636, 2010.
- [5] Krautschik, Ito, et. al "Impact of EUV light scatter on CD control as a result of mask density changes" Proc. of SPIE Vol. 4688 (2002)
- [6] Shiraishi, Oshino, et. al "Flare modeling and calculation for EUV optics" Proc. of SPIE 7636, 763629 (2010)
- [7] Schellenberg, Word, et. al "Layout compensation for EUV flare" Proc. SPIE Vol. 5751 2005

- [8]Jang, Zavyalova, et. al “Requirements and results of a full field EUV OPC flow” Proc. of SPIE Vol. 7271 72711A 2009
- [9] McIntyre et. al. “Modeling and Experiments of Non-Telecentric Thick Mask Effects for EUV Lithography”, Proc. of SPIE Vol. 7171, 2010.
- [10] A.M. Goethals, R. Jonckheere, et. al., “EUV lithography program at IMEC,” Proc. of SPIE Vol. 6517, 2007.
- [11]Adam and Neureuther “Methodology for accurate and rapid simulation of large arbitrary 2D layouts of advanced photomasks” Proc. of SPIE Vol. 4562 (2002)
- [12] K. Adam, M. Lam, “Hybrid Hopkins-Abbe Method for Modeling Oblique Angle Mask Effects in OPC”, Proc. of SPIE Vol. 6924, 2008.
- [13] G. Lorusso, G. Fenger, et. al., “Flare in EUV Lithography: Metrology, Out of Band Radiation, Fractal PSF and Flare Map Calibration”, J. Micro/Nanolith., Oct. 2009.
- [14]Zavyalova, Su, et. al “EUV modeling accuracy and integration requirements for the 16 nm node” Proc. of SPIE Vol. 7636 76327-1 (2010)
- [15]Hendrickx, Lorusso, et. al “Accurate models for EUV lithography” Proc. of SPIE Vol. 7488 74882G-1 (2009)
- [16] Cobb, A. Zakhor, “A mathematical and CAD framework for proximity correction”, SPIE, vol. 2726, p. 208-222, 1996.
- [17] Cobb, “Flexible sparse and dense OPC algorithms”, SPIE vol. 5853, p. 693-702, 2005.